Performance of a direct detection camera for off-axis electron holography

Shery L.Y. Chang [a,b,*], Christian Dwyer [a,c], Juri Barthel [a], Chris B. Boothroyd [a], Rafal E. Dunin-Borkowski [a]

[a] Ernst Ruska-Centre for Microscopy and Spectroscopy with Electrons, and Peter Grünberg Institute, Forschungszentrum Jülich, D-52425 Jülich, Germany
[b] LeRoy Eyring Center for Solid State Science, Arizona State University, Tempe, AZ 85287, USA
[c] Department of Physics, Arizona State University, Tempe, AZ 85287, USA

ABSTRACT

The performance of a direct detection camera (DDC) is evaluated in the context of off-axis electron holographic experiments in a transmission electron microscope. Its performance is also compared directly with that of a conventional charge-coupled device (CCD) camera. The DDC evaluated here can be operated either by the detection of individual electron events (counting mode) or by the effective integration of many such events during a given exposure time (linear mode). It is demonstrated that the improved modulation transfer functions and detective quantum efficiencies of both modes of the DDC give rise to significant benefits over the conventional CCD cameras, specifically, a significant improvement in the visibility of the holographic fringes and a reduction of the statistical error in the phase of the reconstructed electron wave function. The DDC's linear mode, which can handle higher dose rates, allows optimisation of the dose rate to achieve the best phase resolution for a wide variety of experimental conditions. For suitable conditions, the counting mode can potentially utilise a significantly lower dose to achieve a phase resolution that is comparable to that achieved using the linear mode. The use of multiple holograms and correlation techniques to increase the total dose in counting mode is also demonstrated.

© 2015 Published by Elsevier B.V.

1. Introduction

The advent of commercially available direct detection cameras (DDC) for transmission electron microscopy (TEM) offers the capacity to reduce the noise level in images and diffraction patterns to essentially that of the Poisson noise of the electron beam. While conventional charge-coupled device (CCD) cameras used in TEM rely on fibre-optically coupled photons as intermediate signal carriers in order to separate and hence protect the complementary metal-oxide semiconductor (CMOS) technology from the beam electrons, DDCs operate via the production of electron–hole pairs generated directly by the beam electrons impinging on a back-thinned CMOS structure. For sufficiently low dose rates, their design can enable significant improvements in the detective quantum efficiency (DQE) and the modulation transfer function (MTF) compared to conventional CCD cameras [1–3]. Hence, the existing literature on DDCs is predominantly focused on structural biological applications, where obvious advantages are gained under the

necessarily low dose conditions, e.g., typically $<10\,\mathrm{e^-\,\mathring{A}^{-2}}$. For example, DDCs have been utilised for resolving high-resolution structural information in biological materials in cryo-EM [4–6]. Consequently, the characteristics of DDCs at dose rates and spatial resolutions applicable to biological materials are already documented. In many other areas of TEM, the dose rate used is typically of the order of $1000\,\mathrm{e^-\,\mathring{A}^{-2}}$, and the spatial resolution can vary from better than 1 Å to a few nanometers. Hence, in these contexts, which includes off-axis electron holography, there have been no demonstrations of DDCs to the best of our knowledge.

Here, we evaluate the applicability and performance of a DDC for off-axis electron holography in TEM, which is an established technique for measuring the electrostatic and magnetic properties of materials and devices. The technique allows the phase shifts experienced by the electron beam wavefield to be reconstructed and uses them to map the spatially varying electric or magnetic field of the sample. In order to measure the increasingly weaker electric and magnetic fields generated from nanomaterials, it is necessary to improve the resolution of the reconstructed phase for a given spatial resolution. Here we evaluate the phase resolution afforded by employing a DDC and compare it with that obtained

with a conventional CCD camera.

The phase resolution in an electron hologram is governed primarily by two competing factors: the transverse spatial coherence and the electron dose. In the past, improvements in phase resolution have been made with the use of brighter electron sources [7–10] and by increased microscope stability which enables longer exposure times and hence a greater total dose [11]. Greater total doses and hence better phase resolution have also been achieved by combining data from multiple holograms [12–17]. In previous work [18], we reported the optimum dose rate and exposure time to achieve the best phase resolution for a given instrument and spatial resolution. In that work, the instrument was fitted with a conventional CCD camera and it was justifiably assumed that the camera performance was independent of dose rate (within reasonable limits). Since DDCs can offer an improved MTF and DQE, with the caveats that these quantities can be dose-rate dependent and that their optimum performance requires low dose rates, it is the aim of this paper to evaluate the performance of a DDC and discuss its potential for off-axis electron holography.

2. Background

The DDC used in this study is the K2 Summit (Gatan, Inc.). It has 3838×3710 pixels, with a pixel size of 5 µm. The camera can be operated in three different modes: "counting", "super-resolution" and "linear". In the former two modes, the underlying frame rate is 400 Hz (regardless of the frame rate set by the user). In the counting mode at a low dose rate, individual incident electrons are identified and digitised as a discrete count at a particular pixel. Higher dose rates mean that there is a significant probability that more than one electron is incident within a cluster of neighbouring pixels per $1/400$ s frame, and since the counting algorithm used by the K2 cannot distinguish between single or multiple electron events, this results in so-called "coincidence losses". Therefore, the counting mode MTF and DQE are highly dependent on the dose rate. For example, at 1 e$^-$ pixel^{-1} s^{-1} (eps) the DQE at zero spatial frequency is nearly equal to unity, but at 10 eps it decreases by over 14% [3]. The super-resolution mode shares many similarities with counting mode, except for the crucial point that the resolution dictated by the physical pixel size is overcome by using an algorithm that locates the position of incident electrons to sub-pixel accuracy, resulting in images composed of four times as many pixels (7676×7420). This results in a further increase of the MTF compared to counting mode, though the increase is perhaps not as large as would be expected, and occurs at the cost of four times the (already very large) amount of data. Therefore, in this paper we do not explicitly consider super-resolution mode. In contrast to the counting mode, the linear mode of the K2 operates by accumulating the charge carriers generated by the impinging beam electrons during a user-set exposure time, which is then read out to provide an image. The latter mode is somewhat akin to conventional CCD cameras, though the readout time of the K2 is much shorter and does not require beam blanking, which is also a very significant advantage for many applications including electron holography.

Due to its ability to count individual electron events, the counting (and super-resolution) mode of the K2 camera is essentially free of readout noise, except for extremely low dose rates, i.e., $\lesssim 0.1$ eps. For dose rates between 1 and 15 eps, it has been demonstrated to have high MTFs [2]. At dose rates higher than 20 eps, the MTF drops significantly due to coincidence losses [1,3]. In contrast, the linear mode, while not offering the benefits of single electron counting, is capable of dose rates similar to those of a conventional CCD camera, and does not suffer from coincidence losses. In addition, the absence of fibre optics in the DDC means that the pixel-scale distortions usually present in conventional CCD camera images are absent. Hence in the context of off-axis electron holography, the a posteriori correction for such distortions is not required.

In the present work, the performance of the K2 counting and linear modes is directly compared with that of an UltraScan 1000 XP CCD camera (Gatan, Inc). The latter camera has 2048×2048 pixels with a 14 µm pixel size.

3. Methods

The experiments were carried out using a Titan 80-300 FEG-TEM (FEI Co.) operated at 300 kV. The microscope was equipped with an ultra-bright X-FEG electron gun, and two biprisms located in the first and second selected area aperture planes, separated by an "extra lens". Both cameras were mounted on the TEM with the K2 located downstream of the UltraScan. The microscope was operated in the standard mode with the objective lens turned on (as opposed to Lorentz mode where the objective is off). Blank holograms (no specimen) were recorded using the second biprism with the extra lens off (the first biprism was not used). The biprism voltage was set to 150 V, which produces a fringe spacing of 83 pm at the specimen plane. The magnification was 180 kX for the K2 (pixel size corresponding to 16.6 pm at the specimen plane) and 450 kX for the UltraScan (a pixel size of 17.3 pm at the specimen plane). The relative values of these magnifications were chosen to compensate for fact that the two cameras have different physical pixel sizes and are located in different optical planes. Hence, the sideband positions are at 0.20 pixel^{-1} for the K2 and 0.21 pixel^{-1} for the UltraScan, i.e., the number of pixels per holographic fringe is very similar. This enables us to attribute any differences in the camera performances solely to their MTF and DQE performances. The calibrated values of the magnifications enabled us to track and hence correct any drift of the hologram throughout the experiment.

Although the above experimental conditions are suitable for electron holography at high spatial resolution, as described later, our results are applicable to other conditions, e.g., Lorentz mode (objective lens off) conditions suitable for magnetic field measurements.

Details regarding the Fourier processing of holograms can be found in Reference [18].

For simplicity, all of our experiments used round illumination and the beam intensity was varied using the C2 lens excitation only. The electron doses mentioned throughout this paper were calculated from the central regions of the holograms where intensity fluctuations from Fresnel fringes are minimised. For the UltraScan, the conversion of ADC counts to electron counts was calibrated by measuring the beam current using a picoammeter connected to the drift tube of a Gatan Imaging Filter (Gatan Inc.). For the K2 counting mode, the dose rate was read directly from the manufacturer's software default value. For the K2 linear mode, the conversion of analog-to-digital converter (ADC) counts to electron counts was calibrated using a dose rate of 1 eps in counting mode as a reference. Since the software default dose rate that was used is based on an average over many cameras, it is expected to be within 10–15% of the real value of the camera tested. However this is still useful for providing an explanation for the comparison of the two modes of K2 with the CCD camera, as the K2 linear and counting modes were cross-calibrated, and dose rate of the CCD camera was independently calibrated. Hence the ratio of DQEs between the K2 and the CCD camera should still be accurate. Doses are quoted in units of electron counts per unit area at the specimen plane, unless otherwise specified.

Important attributes of the camera for electron holography are

the MTF and DQE. Here we have measured the MTF and DQE independently based on the methods reported previously by Thust [19] and McMullan et al. [1], respectively. For the K2 counting mode, we used a dose rate of 2 eps and a total dose of 3600 e$^-$ pixel^{-1} (1800 s acquisition). Total counts of 9500 e$^-$ pixel^{-1} (40 s acquisition) and 12,870 e$^-$ pixel^{-1} (20 s acquisition) were used for the K2 linear mode and UltraScan, respectively.

4. Theoretical background

Before proceeding to the discussion of results, it is useful to summarise the theory that is most relevant to the discussion. In contrast to our previous work [18], here we attempt to clearly separate the attributes of the electron beam from those of the camera. For this purpose, in this section and the Appendix we often use a subscript "0" to denote quantities before detection by the camera, i.e., not including camera effects. This convention is not needed in other sections.

The phase error, $\Delta\phi$, determines the minimum difference that can be distinguished in the reconstructed phase at a given spatial resolution. Here, we define $\Delta\phi$ as the standard deviation associated with the cosine and the sine of the phase, which has the advantage of remaining well-defined and meaningful for arbitrary doses and in the presence of phase wraps [18]. For sufficiently well-defined phases, this definition coincides with the usual one [20–22].

The statistical phase error in a given pixel in the reconstructed wave function, following Fourier processing of the off-axis hologram, is given by the expression (see Appendix)

$$\Delta\phi = \left(\frac{2a}{N_{\text{eff}}}\right)^{1/2},\tag{1}$$

where $a = A_{\text{sb}}/A_{\text{total}} < 1$ is the ratio of the area enclosed by the sideband mask relative to the total area of Fourier space and N_{eff} is the *effective* number of electrons per pixel that are detected [20,21]. In this work, we define the effective number of electrons before the camera as

$$N_{\text{eff},0} = N_0 V_0^2,\tag{2}$$

where N_0 is the average number of incident electrons per pixel and V_0 is the fringe visibility (fringe contrast) before the camera. The effective number of electrons that are observed is given by

$$N_{\text{eff}} = N_{\text{eff},0} \times \text{DQE}(k_0),\tag{3}$$

where $\text{DQE}(k_0)$ is the camera's DQE at the fringe spatial frequency k_0. The phase error in Eq. (1) is understood as being inversely proportional to the Poisson noise of N_{eff} and scaled according to the loss of spatial resolution that results from masking the sideband. From Eq. (1), it can be readily understood that the minimisation of statistical phase errors in electron holography corresponds to maximising N_{eff}. Camera effects aside, maximising N_{eff}, generally requires a balance between the visibility V_0 and the dose N_0 [18], since the visibility inevitably decreases with increasing dose rate.

The visibility can be described as

$$V_0 = V_0(t) S_0(\hat{N}_0).\tag{4}$$

where $V_0(t)$ is the time-dependent part of the visibility, which arises from instrument instabilities that are slower than the fastest exposure time, and $S_0(\hat{N}_0)$ is the spatial coherence envelope of the wavefield, which includes instabilities faster than the shortest exposure time and is written here as a function of the average

number of incident electrons per pixel per unit time $\hat{N}_0 = N_0/t$. The observed visibility is given by (see Appendix)

$$V = V_0 \times \text{MTF}(k_0),\tag{5}$$

where $\text{MTF}(k_0)$ is the camera's MTF at the fringe spatial frequency k_0.

For a camera whose performance is independent of the dose rate, such as a conventional CCD camera, Eq. (3) is a relatively simple function of $\hat{N}_0$ and t, which allows $\hat{N}_0$ and t to be optimised independently. This property has been used to predict optimum dose and exposure time to obtain minimum phase error for a given spatial resolution [18].

However, a complication arises for a camera whose performance is dose rate dependent, such as the K2 operating in counting mode, where both the DQE and the MTF decrease with increasing dose rate [1–3]. In this case, the DQE in Eq. (3) becomes a function of $\hat{N}_0$, and so the optimisation of dose rate and exposure time that we proposed previously [18] is no longer valid. This will be observed and discussed later in the paper.

5. Results and discussion

5.1. MTF and DQE measurements

To understand what degree of improvement the K2 might afford over the UltraScan, we need to know their MTFs and DQEs. The former describes the attenuation of image contrast as a function of spatial frequency. The latter is defined as the quotient of the squared signal-to-noise ratios at the output and the input of the camera. The comparisons of MTFs and DQEs given here are, of course, applicable to all imaging and diffraction experiments. In the following sections, the discussion will be largely restricted to off-axis electron holography.

Fig. 1(a) compares the MTFs of the K2 counting mode (red), K2 linear mode (blue) and the UltraScan (black). It is immediately apparent that the MTFs for both the linear and counting modes of the K2 are substantially higher than that of the UltraScan across all frequencies, with the counting mode offering dramatic improvements up to Nyquist (and beyond). The MTFs for the K2 counting and linear modes are both comparatively flat, and they do not have the characteristic dip at about 0.1 pixel^{-1} commonly observed in conventional CCD cameras, e.g., the UltraScan. This dip presumably arises from the significant backscattering of the relatively high energy (300 keV) beam electrons by the fibre optics beneath the scintillator [23]. By comparison, the active silicon layer in the K2 is much thinner, and there is no substrate to scatter from. This is largely responsible for its improved MTFs, even though it has a smaller physical pixel size. Similarly, comparison of the DQEs among the three cameras/modes, shown in Fig. 1(b), reveals that the DQE for the K2 counting mode is significantly higher than that of the UltraScan across all spatial frequencies, as expected for the DDC under these dose conditions. The K2 linear mode is also seen to have a substantially better DQE than the UltraScan.

However, it is very important to remember that, of the three cameras/modes compared here, the K2 counting mode is unique in that its performance is highly dose rate dependent. The dose rate (2 eps) used to measure the K2 counting mode's MTF and DQE lies well within this mode's optimum range. Increasing the dose rate beyond 20 eps causes a rapid and drastic reduction in MTF and DQE performance. Hence, in a higher dose rate regime, it is the K2 linear mode that gives the best performance of the three cameras/modes.
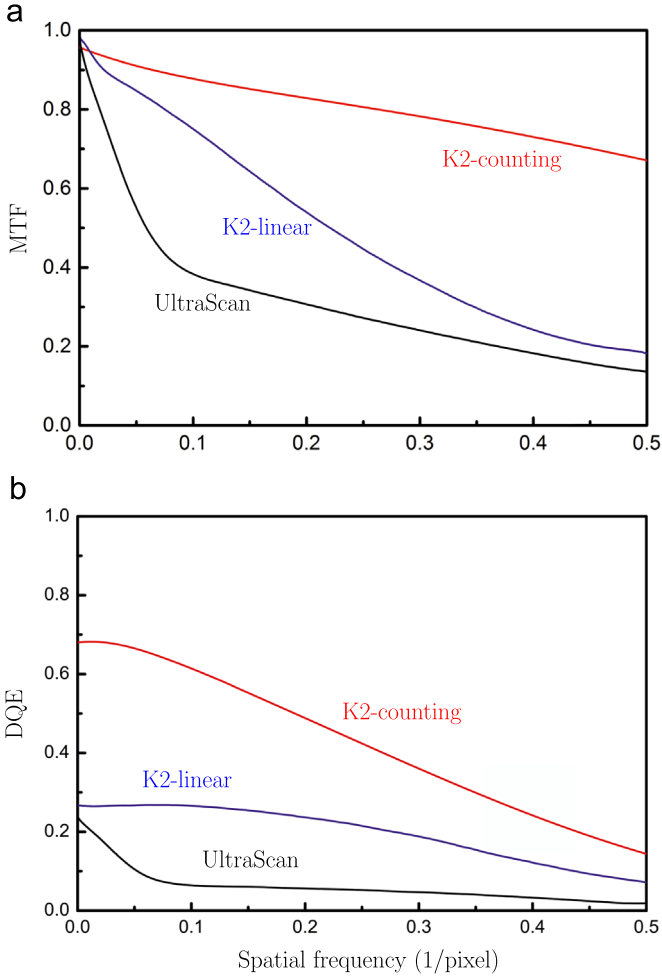
a

b

Fig. 1. (a) Modulation transfer function (MTF) and (b) detective quantum efficiency (DQE) of the UltraScan, K2 linear and counting modes, measured for 300 keV incident electrons. A dose rate of 2 eps was used for the K2 counting mode. The MTFs shown here have had the effects of pixelation removed. (For interpretation of the references to color in this figure caption, the reader is referred to the web version of this paper.)

5.2. Holograms from the K2 and UltraScan cameras

Fig. 2 compares holograms recorded using the K2 counting mode and the UltraScan for an average dose of <2 electrons per pixel (measured from the central region of the hologram). To ensure a fair comparison, the dose, exposure time, and pixel sampling are the same or very similar for both cameras (note that the K2 captures a larger field of view since it has more pixels). It can be readily seen that the hologram fringes from the K2 have much higher contrast and less noise than those from the UltraScan. More specifically, a delocalisation of the fine scale detail is much more apparent in the UltraScan, and presumably arises because of the more significant sideways scattering of beam electrons in the scintillator. The latter observation is in line with the UltraScan's poorer MTF as shown in Fig. 1(a). In addition, the UltraScan gives rise to considerable horizontal streaking (readout noise), which appears to be different in each of its four quadrants. By comparison, readout noise from the K2 is barely discernible at this dose rate (though its readout noise does become apparent at both very low dose rates, i.e., ≲0.1 eps, and dose rates higher than 20 eps). Linescans taken across the hologram fringes readily demonstrate the significantly higher fringe contrast from the K2, and since the dose rate and hence the transverse spatial coherence of the beam is very similar for both cameras, the observed differences directly reflect the camera performances under these low dose conditions.

5.3. Comparisons of fringe visibility and phase error

In order to judge quantitatively the performance of the K2 camera for off-axis electron holography, we compare the fringe visibility and phase error obtained from the K2 counting mode, the K2 linear mode and the UltraScan. Once again, we have set the optical conditions to be as close as possible to ensure that the comparisons reflect the differences in camera/mode performance.

Fig. 3(a) shows the observed fringe visibilities (including camera effects) plotted as a function of the incident dose rate. In each of the three cases, the fringe visibilities show an overall decrease with increasing dose rate. This is entirely expected since an increased dose rate implies a loss of spatial coherence. On the other hand, a comparison of the fringe visibilities at the same dose rate reflects the different MTF performances of the cameras/modes. For lower dose rates ($<14 \times 10^2 \, e^-/\text{Å}/s$), the visibility from the K2 counting mode is far superior to the other modes. However, for higher dose rates ($>18 \times 10^2 \, e^-/\text{Å}/s$), the visibility from the K2 counting mode quickly falls due to coincidence losses and begins to approach that of the K2 linear mode. The incident dose rate at which the visibility begins to decrease anomalously is 40 eps, as indicated by a red arrow in Fig. 3(a). This is also the upper limit of the dose rate recommended by the manufacturer for this mode (readers are reminded that the dose rate measured at the central region of the hologram is about 2 times that in the vacuum region). Hence it is the K2 linear mode that produces the highest visibility in the higher dose regime.

In order to confirm our expectation that the differences in the observed visibilities reflect the differences in the MTFs, we can estimate the expected improvement using Eq. (5). For dose rates applicable to the MTF measurements in Fig. 1(a), we expect $V_{K2}/V_{US} \approx \text{MTF}_{K2}/\text{MTF}_{US}$. Given that the sidebands occur at $0.20 \, \text{pixel}^{-1}$ and $0.21 \, \text{pixel}^{-1}$ for the K2 and UltraScan, respectively, the measured ratios of the MTFs are $\text{MTF}_{K2,C}/\text{MTF}_{US} \approx 2.77$ and $\text{MTF}_{K2,L}/\text{MTF}_{US} \approx 1.80$. By comparison, the measured ratios of the visibilities are $V_{K2,C}/V_{US} \approx 2.80$ and $V_{K2,L}/V_{US} \approx 1.94$. Hence these results confirm our expectations.

Fig. 3 (b) shows the corresponding measurements of the phase errors. The phase error is determined by the Poisson noise in the effective signal N_{eff}, which, as understood from Eqs. (2) and (3), is comprised of three factors: the incident dose, the fringe visibility, and the camera's DQE. The dose and the visibility are competing. That is, higher doses can give a higher N_{eff} and hence result in lower phase errors, but lower dose rates can also increase N_{eff} through better spatial coherence/fringe visibility and hence give lower phase errors. The result is that there is an optimum dose rate that gives a minimum phase error. This is observed for both the K2 linear mode and the UltraScan, where the optimum dose rate is about $6 \times 10^3 \, e^-/\text{Å}^2/s$ for these conditions. For the K2 counting mode, we also observe a minimum phase error, though it occurs "prematurely" at a dose rate of about $1.4 \times 10^3 \, e^-/\text{Å}^2/s$ (40 eps) due to the rapid degradation of the DQE with increasing coincidence losses. Note that for dose rates greater than about 50 eps the K2 linear mode outperforms the K2 counting mode, even though the visibility in linear mode is lower (Fig. 3(a)). This indicates that, in counting mode, increasing the dose rate beyond the recommended range causes the DQE to degrade faster than the MTF.

Similarly, we can confirm that the improved phase errors reflect the improved DQEs. For dose rates applicable to the DQE measurements, we expect $\Delta\phi_{K2}/\Delta\phi_{US} = \{\text{DQE}_{US}/\text{DQE}_{K2}\}^{1/2}$. The ratios of the phase errors are $\Delta\phi_{K2,C}/\Delta\phi_{US} \approx 0.35$ and $\Delta\phi_{K2,L}/\Delta\phi_{US} \approx 0.45$. By comparison, $\{\text{DQE}_{US}/\text{DQE}_{K2,C}\}^{1/2} \approx 0.33$ and
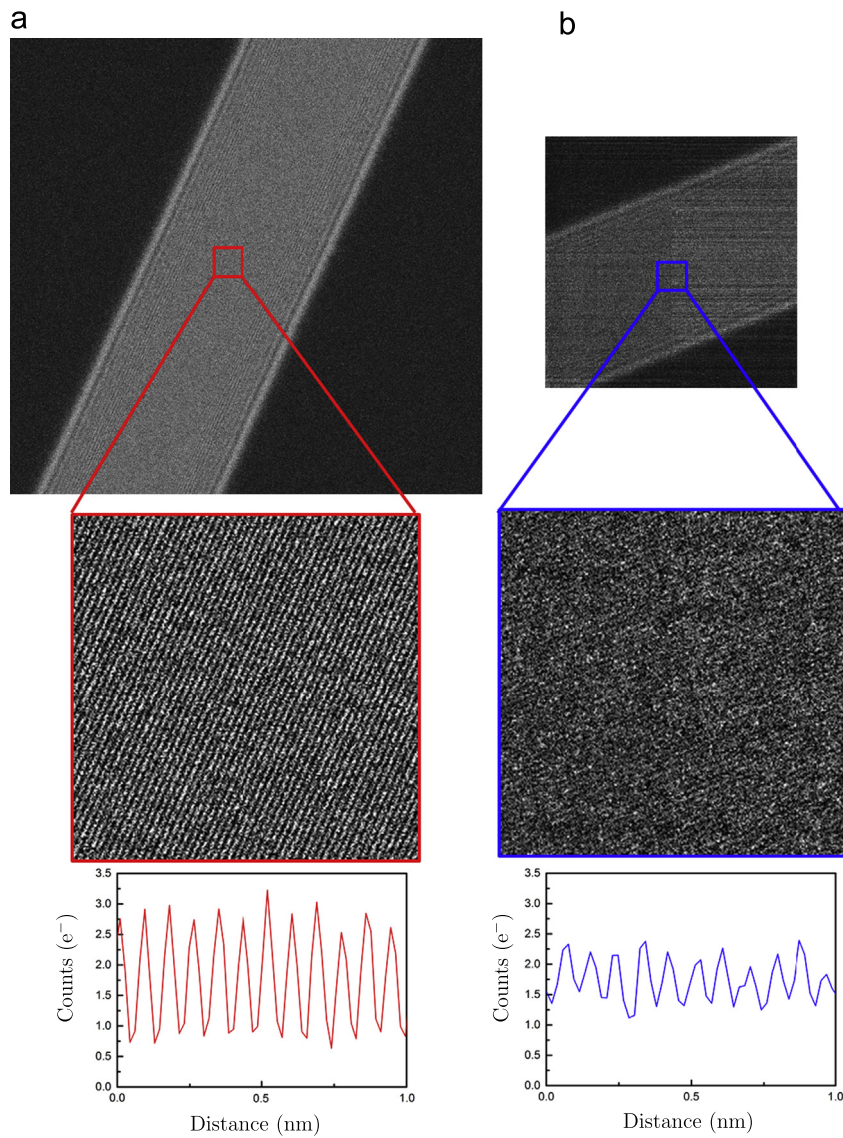
Fig. 2. Holograms of similar dose and the corresponding linescans across the centre taken using (a) the K2 camera counting mode, and (b) the UltraScan camera. Both holograms were taken with a biprism voltage of 150 V and an exposure time of 1 s. The pixel samplings correspond to 16.6 pm/pixel (K2) and 17.3 pm/pixel (US) at the specimen plane. The dose rates were 1.8 eps (K2) and 1.6 eps (US).
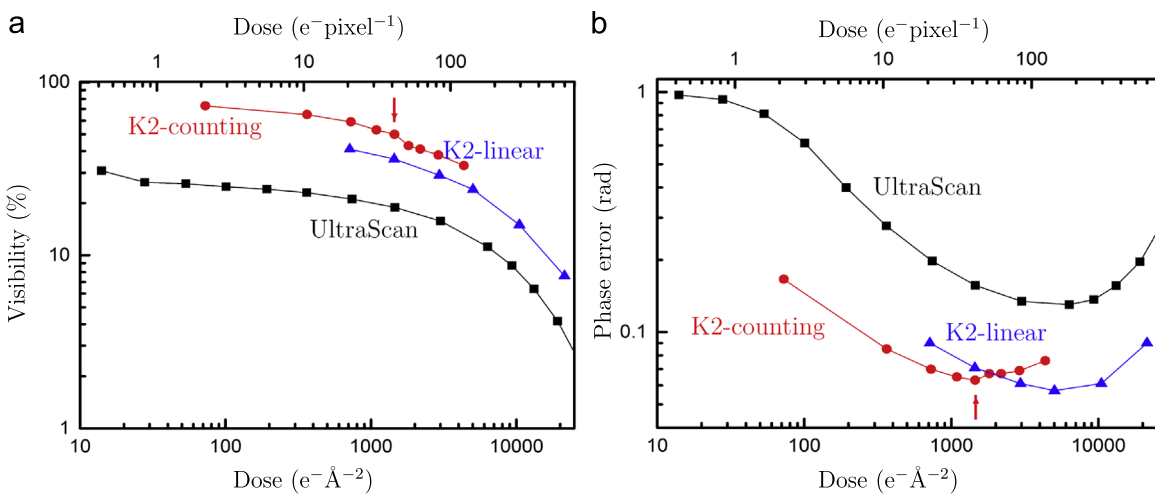

Fig. 3. (a) Observed fringe visibilities V, and (b) phase errors $\Delta\phi$ as a function of dose using UltraScan (black squares), K2 linear mode (blue triangles) and K2 counting mode (red circles). The biprism voltage, exposure time and pixel samplings match Fig. 2. The red arrow indicates the dose rate for the counting mode where the minimum phase error occurs. (For interpretation of the references to color in this figure caption, the reader is referred to the web version of this paper.)

$\{DQE_{US}/DQE_{K2,L}\}^{1/2} \approx 0.48$, in good agreement.

These results for the phase errors nicely reveal the potential advantages of the K2 camera in the context of off-axis electron holography. Firstly, we observe that the K2 linear mode simply and directly gives a phase error that is significantly smaller than the UltraScan, due to its better DQE. In the context of traditional holography experiments, where higher dose rates tend to be used for practical reasons, the K2 linear mode therefore offers a significant advantage. This will be particularly useful for experiments such as magnetic field measurements, which generally demand smaller phase errors. Secondly, and perhaps most excitingly, in Fig. 3(b) we observe that the K2 counting mode achieves a minimum phase error that is significantly smaller than the UltraScan and nearly as small as the K2 linear mode, but with 4 times lower dose! (Note that the actual numbers depend on the specific condition, e.g., the magnification, but the trends observed between the different cameras/modes will persist in other conditions.) The latter observation opens the door to "low-dose electron holography", where, despite the low dose, good phase resolution might still be obtained through the combination of higher spatial coherence and a significantly improved DQE.

5.4. Choice of counting vs. linear mode

Although the above discussion is based on the results obtained for a given optical condition, our investigation can give recommendations for other conditions. We have shown previously [18] that the dose rate that minimises the phase error in a single hologram can be predicted for any given combination of biprism voltage and magnification, either in standard or Lorentz mode, based on one reference series of holograms taken using an exposure time short enough to neglect instrument instabilities. The predicted optimum dose rate is given by the simple relationship

$$\hat{N} = \left(\frac{w_{ref}/\delta_{ref}}{w/\delta} \right)^2 \hat{N}_{ref}, \tag{6}$$

where $\hat{N}$, w and δ are the new optimum dose rate, hologram interference width (determined by the biprism voltage and biprism defocus) and pixel sampling at the specimen plane (determined by the magnification), respectively, and $\hat{N}_{ref}$, w_{ref} and δ_{ref} are the corresponding values from the reference series. If the reference series is taken using the K2, then linear mode should be used. Eq. (6) is readily applicable to give a new optimum dose rate in K2 linear mode, as its DQE is dose-rate independent.

For the K2 counting mode, Eq. (6) is applicable up to a point: if $\hat{N}$ turns out to be below 40 eps, where variations in the DQE are relatively small (approximately less than 15% [2]), then Eq. (6) applies. Otherwise if $\hat{N} > 40$ eps, it is advantageous to use the linear mode. This is exemplified in Table 1.

Table 1

Optimum dose rate $\hat{N}_{opt}$ and the corresponding recommended camera mode for a selection of experimental conditions using the K2 camera. M is the magnification, V_{BP} is the biprism voltage. δ and w are the pixel size and the interference width measured at the specimen plane, respectively.

Microscope mode	M	δ (pm)	V_{BP} (V)	w (nm)	$\hat{N}_{opt}$ (eps)	Camera mode
Standard	180k	16.6	150	31	140*	Linear
Standard	360k	8.1	150	31	33	Counting
Lorentz	24.5k	232	150	364	140	Linear
Lorentz	24.5k	232	87	176	600	Linear

* The value marked "*" indicates the reference measurement.

6. Beyond a single hologram

Based on our experience, as well as on the recommendations of the manufacturer, it is clear that the advantages of the K2 counting mode lie entirely in the lower dose rate regime, i.e., <40 eps. If we try to improve the phase error in the counting mode, not by increasing the dose rate, but by using a longer exposure time, we eventually run into limitations set by the instrument's holographic stability lifetime (in practice due to drift of the hologram and/or specimen). To overcome this limitation, we have acquired a series of holograms totalling 120 s exposure at the optimum dose rate ($\sim 14 \times 10^2$ e$^-$/Å^2/s), using a 1 s exposure time for each hologram (i.e., 120 holograms). This approach enables us to track the drift in the hologram fringes using correlation techniques. We find that, despite the relatively low dose in each hologram, a simple cross-correlation of the holograms can produce very robust results, provided that a sufficiently large area is used for the correlation (here we used an area of 512×512 pixels). Fig. 4 shows the phase errors of individual holograms and those of cumulated cross-correlated holograms up to 120 s total exposure time. While the phase error of individual holograms fluctuates around 0.063 rad ($\sim 2\pi/100$), the cross-correlated holograms exhibit a reduced phase error approximately following an ideal $1/\sqrt{n}$ trend, where n is the number of holograms. The phase error after averaging over 120 s of holograms is 0.008 rad ($\sim 2\pi/800$), an 8-fold improvement over a single hologram, which compares very well with the 11-fold improvement expected in the ideal case. In addition to the advantages of better spatial coherence and camera performance mentioned above, a further advantage of acquiring multiple holograms in counting mode is that the dose for each hologram is low so that dose-rate-dependent specimen damage can be reduced. Furthermore, as there is effectively no readout time in counting mode, the total acquisition time is equal to the total exposure time, which again minimises problems arising from instrument and specimen drift and dose-dependent specimen damage.

7. Conclusions

We have demonstrated that a direct detection camera (here the Gatan K2 Summit) can offer significantly better performance in
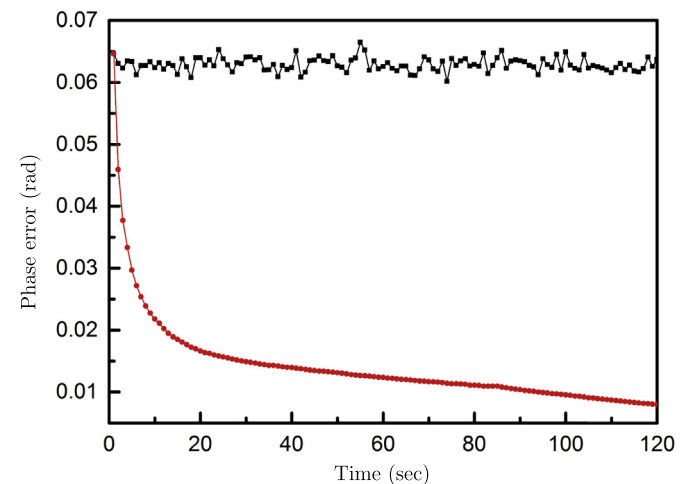

Fig. 4. Phase errors of individual holograms (black) and cross-correlated holograms (red) recorded over a time span of 120 s. Each hologram is recorded with an exposure time of 0.2 s, using the optimum dose rate shown in Fig. 3(b). (For interpretation of the references to color in this figure caption, the reader is referred to the web version of this paper.)

electron holography compared to a conventional scintillator-based CCD camera (here the Gatan UltraScan 1000 XP). For a given spatial resolution, we have demonstrated an at-least two-fold improvement in phase errors using the counting and linear modes of the K2. This improvement has been confirmed to be due to the better DQE of the K2.

As the statistical phase error in electron holography is governed by a competition between spatial coherence and dose, we found that the linear and counting modes of the K2 are both advantageous, though in different dose regimes. The linear mode, which can handle much higher dose rates, enables the dose rate (and exposure time) to be optimised to give the best phase error in a single hologram. This is ideally suited to experiments that seek to measure magnetic fields, for example, where accurate results rely on an ability to observe small differences between individual phase measurements taken under opposite magnetisations of the specimen.

On the other hand, while the counting mode can be used only at lower dose rates, its better MTF and DQE could offer advantages for high-spatial-resolution holography. For the conditions used here, it was shown that the better DQE, coupled with the higher spatial coherence of the electron beam at lower dose rates, achieved a phase error nearly as good as the (optimised) linear mode but with significantly less dose (4 times for the conditions used here). Hence the K2 counting mode also offers the very exciting possibility to perform "low dose electron holography" on radiation-sensitive specimens.

Taking full advantage of the K2 counting mode to perform dose-efficient holography will likely require the use of multiple holograms and correlation techniques. To this end, we demonstrated that cross correlation of a series of holograms taken using the K2 counting mode can produce robust results approaching the ideal $\sqrt{n}$ improvement in the phase error, despite the relatively low dose in each hologram. Hence, by spreading the dose over a longer total acquisition time (that is, slowing down the holography experiment) and compensating for instrument instabilities using correlation techniques, we gain in terms of both spatial coherence and detector performance. If this method is applied to high-resolution holography, where specimen drift is often a serious issue, the lack of readout time will be a further benefit in minimising these instabilities and any dose-dependent specimen damage.

Appendix A

In this appendix we derive the manner in which the detector MTF and DQE affect the fringe visibility and the phase error in electron holography.

The fundamental properties of a CCD camera stem from the manner in which the specific paths followed by the incident electrons inside the camera contribute to the detected signal. To this end, let the signal detected at position x, due to an incident electron entering the camera at position x_0 and following a specific path which we label μ, be given by the function $g_\mu(x - x_0)$. The dependence on the difference $x - x_0$ assumes homogeneity. If we denote the probability of path μ by $d\mu$, then the average signal of an electron entering at x_0 is $\int d\mu \, g_\mu(x - x_0)$. If $P(x)$ denotes the probability distribution of the incident electrons entering the camera, then the expectation value and variance of the Fourier transformed signal are given by [23]

$$\langle \tilde{I}(k) \rangle = \tilde{P}(k) \int d\mu \, \tilde{g}_\mu(k), \tag{7}$$

and

$$|\Delta \tilde{I}(k)|^2 = \tilde{P}(0) \int d\mu |\tilde{g}_\mu(k)|^2, \tag{8}$$

where the tildes denote Fourier-transformed quantities. Here the variance applies to the modulus of the complex deviations $\Delta \tilde{I}(k)$; the phase of the deviations are uniformly random on $[0, 2\pi)$. For real cameras, which are both pixellated and finite in area, it is most convenient to use discrete Fourier transforms, i.e., for an arbitrary function $f(x)$

$$\tilde{f}(k) = \sum_x f(x) e^{-2\pi i k \cdot x}, \quad f(x) = \frac{1}{M} \sum_k \tilde{f}(k) e^{+2\pi i k \cdot x}, \tag{9}$$

where k is a wave vector allowed by the periodic boundary conditions and M is the number of camera pixels.

For a set of holographic fringes with spacing k_0^{-1}, the probability $\tilde{P}(k)$ can be written

$$\tilde{P}(k) = MN_0 \left(\delta_k + \frac{V_0}{2} \delta_{k-k_0} + \frac{V_0}{2} \delta_{k+k_0} \right), \tag{10}$$

where N_0 is the average number of incident electrons per pixel, V_0 is the visibility (contrast) of the fringes before detection, and δ_k is the Kronecker delta symbol which equals unity when $k=0$ and vanishes otherwise. Hence the detected visibility of the fringes is

$$V = \frac{2\langle \tilde{I}(k_0) \rangle}{\langle \tilde{I}(0) \rangle} = V_0 \frac{\int d\mu \, \tilde{g}_\mu(k_0)}{\int d\mu \, \tilde{g}_\mu(0)} = V_0 \times \mathrm{MTF}(k_0), \tag{11}$$

where $\mathrm{MTF}(k)$ is the modulation transfer function of the camera. That is, the fringe visibility is reduced by the MTF.

During the holographic reconstruction, the process of applying a circular mask to the sideband at $+k_0$ and shifting it back to the origin gives rise to the following expectation value and variance

$$\langle \tilde{I}(k) \rangle = \frac{MN_0 V_0}{2} \delta_k \int d\mu \, \tilde{g}_\mu(k_0), \tag{12}$$

and

$$|\Delta \tilde{I}(k)|^2 = MN_0 H(k_r - |k|) \int d\mu |\tilde{g}_\mu(k + k_0)|^2, \tag{13}$$

where $H(k)$ is the Heaviside step function and k_r the mask radius. For simplicity we neglect the variation of the quantity $\int d\mu |\tilde{g}_\mu(k)|^2$ within the sideband mask, in which case the variance can be approximated as

$$|\Delta \tilde{I}(k)|^2 \simeq MN_0 H(k_r - |k|) \int d\mu |\tilde{g}_\mu(k_0)|^2. \tag{14}$$

Taking the inverse Fourier transform yields a reconstructed wave function with expectation value and variance given by

$$\langle \psi(x) \rangle = \frac{N_0 V_0}{2} \int d\mu \, \tilde{g}_\mu(k_0), \tag{15}$$

and

$$|\Delta \psi(x)|^2 \simeq \frac{mN_0}{M} \int d\mu |\tilde{g}_\mu(k_0)|^2, \tag{16}$$

where m is the number of pixels inside the sideband mask and, again, the variance refers to the modulus of the deviation while the phase of the deviation is random on $[0, 2\pi)$. Note that $\tilde{g}_\mu$ enters into Eqs. (15) and (16) analogously to Eqs. (7) and (8).

The variance of the reconstructed wave function gives rise to a circular "cloud" in the complex plane centred at the expectation value $\langle\psi(x)\rangle$. Provided that the "cloud" does not lie too close to the origin, the variance in the phase of the reconstructed wave function can be calculated using a small-angle approximation, yielding

$$(\Delta\phi)^2 \simeq \frac{|\Delta\psi(x)|^2/2}{|\langle\psi(x)\rangle|^2} = \frac{2a}{N_0 V_0^2} \frac{1}{DQE(k_0)}. \tag{17}$$

where $a = m/M$ and $DQE(k)$ is the detective quantum efficiency, defined by

$$DQE(k) = \frac{|\int d\mu\, \tilde{g}_\mu(k)|^2}{\int d\mu\, |\tilde{g}_\mu(k)|^2}. \tag{18}$$

From the Schwarz integral inequality, it follows that $DQE(k) \le 1$, and that $DQE(k) = 1$ is achieved if and only if $\tilde{g}_\mu(k)$ is independent of μ. Hence a real detector must have $DQE(k) < 1$, which inevitably amplifies the phase error.

Traditionally, the DQE describes the reduction in the squared signal-to-noise ratio caused by the camera. Hence the appearance of the DQE can be understood intuitively by noting that the phase error $\Delta\phi$ can be considered to be the inverse of a signal-to-noise ratio, where $|\langle\psi(x)\rangle|$ is the signal and $|\Delta\psi(x)|/\sqrt{2}$ is the noise.

References

[1] G. McMullan, A. Faruqi, R. Henderson, N. Guerrini, R. Turchetta, A. Jacobs, G. van Hoften, Ultramicroscopy 109 (2009) 1144.
[2] R.S. Ruskin, Z. Yu, N. Grigorieff, J. Struct. Biol. 184 (2013) 385.
[3] G. McMullan, A. Faruqi, D. Clare, R. Henderson, Ultramicroscopy 147 (2014) 156.
[4] X. Li, P. Mooney, S. Zheng, C.R. Booth, M.B. Braunfeld, S. Gubbens, D.A. Agard, Y. Cheng, Nat. Method 10 (2013) 584.
[5] B. Bammes, R. Rochat, J. Jakana, D. Chen, W. Chiu, J. Struct. Biol. 177 (2012) 589.
[6] A. Milazzo, A. Cheng, A. Moeller, D. Lyumkis, E. Jacovetty, J. Polukas, M. Ellisman, N. Xuong, B. Carragher, C. Potter, J. Struct. Biol 176 (2011) 404.
[7] M. Linck, B. Freitag, S. Kujawa, M. Lehmann, T. Niermann, Ultramicroscopy 116 (2012) 13.
[8] B. Freitag, G. Knippels, S. Kujawa, P.C. Tiemeijer, M. Van der Stam, D. Hubert, C. Kiesielowski, P. Denes, A. Minor, U. Dahmen, in: Proceedings of EMC: Instruments and Methods, vol. 1, 2008, p. 55.
[9] D.C. Joy, Y.S. Zhang, T. Hashimoto, R.D. Bunn, Ultramicroscopy 51 (1994) 1.
[10] M. Lehmann, Ultramicroscopy 100 (2004) 9.
[11] D. Cooper, R. Truche, P. Rivallin, J.M. Hartmann, F. Laugier, F. Bertin, A. Chabli, J.L. Rouviere, Appl. Phys. Lett. 91 (2007) 143501.
[12] E. Voelkl, Ultramicroscopy 110 (2010) 199.
[13] R.A. McLeod, M. Bergen, M. Malac, Ultramicroscopy 141 (2014) 38.
[14] T. Niermann, M. Lehmann, Micron 63 (2014) 28.
[15] Q. Ru, J. Endo, T. Tanji, A. Tonomura, Appl. Phys. Lett. 59 (1991) 2372.
[16] K. Yamamoto, I. Kawajiri, T. Tanji, M. Hibino, T. Hirayama, J. Electron. Microsc. 49 (2000) 31.
[17] T. Suzuki, S. Aizawa, T. Tanigaki, K. Ota, T. Matsuda, A. Tonomura, Ultramicroscopy 118 (2012) 21.
[18] S.L.Y. Chang, C. Dwyer, C.B. Boothroyd, R.E. Dunin-Borkowski, Ultramicroscopy 151 (2015) 37.
[19] A. Thust, Phys. Rev. Lett. 102 (2009) 220801.
[20] H. Lichte, K.H. Herrmann, F. Lenz, Optik 77 (1987) 135.
[21] W.J. de Ruijter, J.K. Weiss, Ultramicroscopy 50 (1993) 269.
[22] A. Harscher, H. Lichte, Ultramicroscopy 64 (1996) 57.
[23] R.R. Meyer, A.I. Kirkland, Micros. Res. Tech. 49 (2000) 269.